

Application of the Hough transform for the automatic determination of soot aggregate morphology

Igor Grishin,¹ Kevin Thomson,² Francesca Migliorini,² and James J. Sloan^{1,*}

¹University of Waterloo, Waterloo, Ontario, N2L 3G1 Canada

²National Research Council of Canada, 1200 Montreal Road, Ottawa, Ontario, K1A 0R6, Canada

*Corresponding author: sloanj@uwaterloo.ca

Received 29 June 2011; revised 25 October 2011; accepted 28 October 2011;
posted 31 October 2011 (Doc. ID 150175); published 8 February 2012

We report a new method for automated identification and measurement of primary particles within soot aggregates as well as the sizes of the aggregates and discuss its application to high-resolution transmission electron microscope (TEM) images of the aggregates. The image processing algorithm is based on an optimized Hough transform, applied to the external border of the aggregate. This achieves a significant data reduction by decomposing the particle border into fragments, which are assumed to be spheres in the present application, consistent with the known morphology of soot aggregates. Unlike traditional techniques, which are ultimately reliant on manual (human) measurement of a small sample of primary particles from a subset of aggregates, this method gives a direct measurement of the sizes of the aggregates and the size distributions of the primary particles of which they are composed. The current version of the algorithm allows processing of high-resolution TEM images by a conventional laptop computer at a rate of 1–2 ms per aggregate. The results were validated by comparison with manual image processing, and excellent agreement was found. © 2012 Optical Society of America

OCIS codes: 100.4994, 180.0180.

1. Introduction

The morphology of submicrometer aerosols affects most of their behaviors and properties from agglomeration and growth to effects on atmospheric radiative transfer [1] and public health [2,3]. This is particularly true of soot particles because of their wide variety of shapes and fractal dimensions. Primarily, fresh soot particles have different characteristics depending on the combustion conditions [4–6], but these initial characteristics are usually modified soon after emission by atmospheric processing [7–10]. Because aged soot particles have such a wide variety of microphysical and chemical properties [11–14], they are difficult to characterize and classify.

A wide variety of methods has been developed to characterize soot particles [15], and while many of these focus on the particle morphology [11,16–18], no

currently available approach can measure the morphology directly. Knowledge of the morphology, however, is crucial for prediction of the atmospheric effects of soot. For example, it is widely believed that the size of soot particles is an important determinant of their toxicity, but the relationship between the aerodynamic size of a soot particle and its fractal dimension makes the size determination difficult without knowledge of the morphology. While useful generalizations of this relationship can be drawn from manual measurements of small samples of particles produced under specific, well-defined conditions [19–21], it is not feasible to use this approach with soot particles in the natural atmosphere because collecting statistics on such a wide variety of particles that differ in sources, histories, and processing environments is prohibitively expensive.

The ability to characterize soot particles is also important because of their effect on cloud nucleation in the atmosphere, which also depends on their characteristics and processing history [22]. Atmospheric

processing of soot particles changes their surfaces from hydrophobic to hydrophilic, which increases their uptake of water vapor and hence their ability to nucleate clouds [23]. The resulting indirect effects of the processed soot aerosols on atmospheric radiative transfer have significant ramifications for climate change.

Because of the wide variability in their shapes, it is necessary to measure large numbers of atmospheric soot particles in various states of processing to get adequate statistics to describe their behavior, for example, in models. Manual methods are too cumbersome and expensive for this purpose, so automated methods are required. Because the morphology of the primary particles and the sizes of the aggregates vary with their sources [24] and extent of processing in the atmosphere [25], the automated method must, at a minimum, be capable of determining the size and morphology. There are at present no automated methods capable of providing this information.

It is well established that soot particles are aggregates of near-spherical primary particles about 10–20 nm in diameter. Transmission electron microscope (TEM) images of these primary particles show that they are assembled in extremely complex geometries that can be described by a fractal power law:

$$N = k \left(\frac{R_g}{a} \right)^D, \quad (1)$$

where N is the number of primary particles in the aggregate, a is the radius of a primary particle, R_g is the radius of gyration of the aggregate, D is the fractal dimension of the aggregate, and k is the fractal prefactor.

Presently, TEM image analysis remains the best method to provide morphological information on soot particles because it gives the geometry of the particles directly, in contrast to indirect methods that rely on related properties such as cooling, aerodynamic mobility, and light scattering. The main disadvantage of TEM imaging, however, is the lack of image processing algorithms capable of measuring the individual primary particles on the soot aggregates rapidly and accurately. While there is much current work on the relationship between the 2D projections of aggregates and their 3D morphology, current methods to characterize the primary particles rely on manual calibrations based on relatively small samples and also involve various assumptions (e.g., that the primary particles are monodisperse). As a result, the majority of existing image processing techniques [26,27] follow a basic method that was introduced by Samson *et al.* [28], which relies on heuristically adjusted parameters or statistically derived constants.

In order to provide a more rapid and flexible method for soot characterization that can be applied quickly to a wide variety of samples, we have developed a fast automated image processing technique that obtains geometric information by analyzing

the TEM images of individual soot aggregates. This novel method uses shape recognition algorithms to retrieve the size distributions of the primary particles that compose the aggregates as well as the sizes of the aggregates themselves. In the following, we will describe the algorithms and use them to analyze TEM images of laboratory-created soot samples. We will also compare the results obtained using the automated procedures with those obtained by manual processing of the same images.

2. Experimental Technique

Thermophoretic sampling and TEM analysis were performed in a nonpremixed ethylene/air flame produced by a Gülder laminar coannular burner, which consists of a central steel fuel nozzle with an inside diameter (i.d.) of 10.9 mm and a coannular tube with an i.d. of 88 mm for the surrounding air [29]. This flame has been widely investigated in the literature. Nonpremixed combustion is of particular interest because it is the regime usually encountered in practical combustion devices such as diesel engines or gas turbines. The air flow rate was 284 liters/min, and the fuel flow rate was 0.194 liters/min, at 20 °C and atmospheric pressure, resulting in a visible flame height of about 65 mm. Thermophoretic sampling was achieved using a probe to which carbon-film-coated copper TEM grids (3 mm diameter) were attached. The probe insertion, exposure, and withdrawal were controlled by a double-acting pneumatic cylinder system that permits adjustable sampling time. In this study, the sampling time in the flame was set to 25 ms.

The sampling locations were on burner centerline at 50 mm above the exit of the fuel tube. Three grids were collected at each location and subsequently imaged with a TEM (Philips CM20) operating at 120 kV. The images were recorded at two different magnifications: 5600× in order to have a significant number of aggregates in a single image and 17,000× to have a better resolution for the identification of the primary particles. Images were captured on a CCD detector with an array size of 2048 × 2048 pixels with a native dynamic range of 16 bit. The image magnifications were 1.62 nm/pixel and 0.63 nm/pixel for the low- and high-magnification measurements, respectively. For the lower magnification, 76 images were acquired; these are designated data array A. For the higher magnification, 21 images were acquired; these are designated data array B. Sample images for each array are shown in Fig. 1. The aggregate in Fig. 1(b) is used to demonstrate the image processing methods discussed in the following section.

Several images were processed manually using commercial software (Image-Pro Plus 4.5.1), which provides the x and y position of a particle's center, together with its area and radius. Only particles having a clear border were selected for this analysis. Images at both magnifications were analyzed, and the comparison of the results with those from the

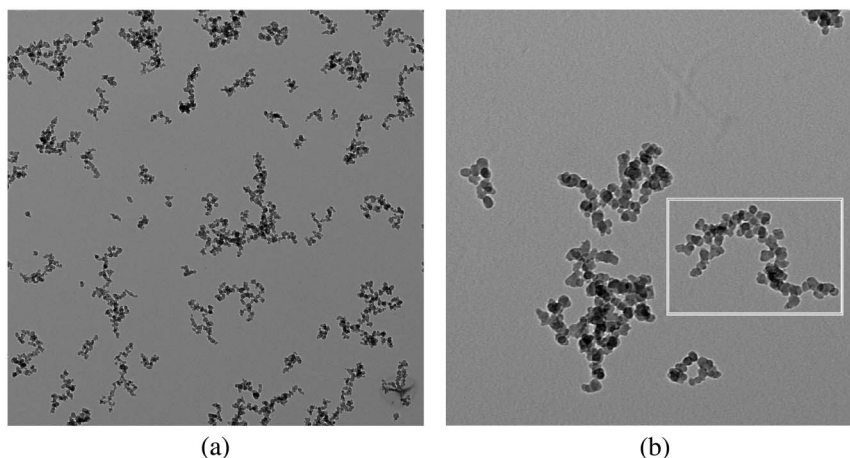


Fig. 1. Examples of TEM images: (a) from data array *A*, magnification 1.62 nm/pixel and (b) from data array *B*, magnification 0.63 nm/pixel. The aggregate in the white box is used to demonstrate the image processing methods.

automated image analysis is reported in the following sections.

3. Automated Image Processing

The 16 bit images were converted to 8 bits as the first step of the image processing. Next, an intensity threshold was applied. Because the images have different background levels induced by differences in the thickness of the carbon film, which supports the soot aggregates, the automatic thresholding based on the Otsu algorithm [30,31] was used to extract the threshold values for each image individually. The choice of the Otsu thresholding method in comparison with other popular techniques (for example, adaptive or entropy thresholding [32]) was mainly determined by its efficiency for large numbers of images.

Otsu thresholding is based on minimization of the intraclass difference within two classes of pixels: background and foreground. The search for the minimum is performed by the analysis of the relative

frequencies of the pixel intensities obtained from the intensity histogram, shown in Fig. 2. In general, the threshold values of the images fell in the range of [130, 160] counts. For the image histogram shown in Fig. 2, the calculated value of the Otsu threshold was 142.

In the next stage of the processing, all aggregates that touch the border of the image were removed and to eliminate irregularities on the image background that interfere with aggregate recognition, a rolling-ball transform was applied. This is based on morphological smoothing operators (so-called *opening* and *closing* [33,34]), which are circular structural elements ranging in size from 5×5 to 7×7 pixels, as shown in Fig. 3. Figure 4(b) shows the result of applying a 6×6 threshold to the TEM image of the selected aggregate in Fig. 1(b).

The 6×6 pixel smoothing element was chosen on the following basis. It is necessary and sufficient that the diameter of the smoothing element satisfy two criteria: it must be large enough to eliminate meaningless noise in the contours of the primary particles, while being small enough to avoid distorting the shapes of the contours. The results of numerical experiments with 5×5 , 6×6 , and 7×7 pixel smoothing elements are reported in Fig. 5. This shows that a small amount of noise remains when the 5×5 element is used, but the 6×6 and 7×7 elements yield smooth distributions. Moreover, the 6×6 and 7×7 elements both produce identical distributions. Thus the 6×6 element satisfies the above criteria, so it

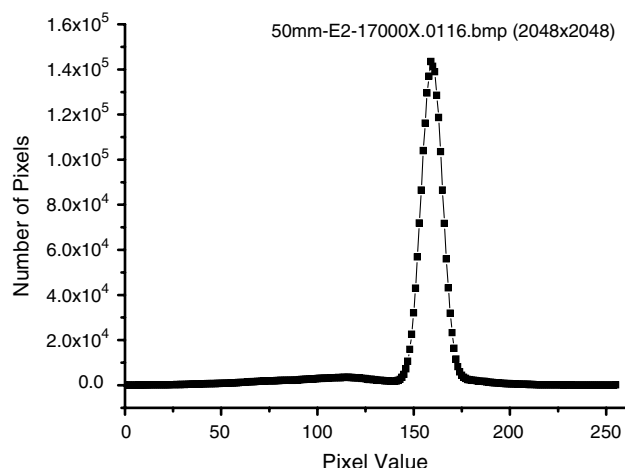


Fig. 2. Intensity histogram of the aggregate image selected in Fig. 1(b). A pixel value of zero corresponds to black; the peak at about 160 represents the most common background intensity value.

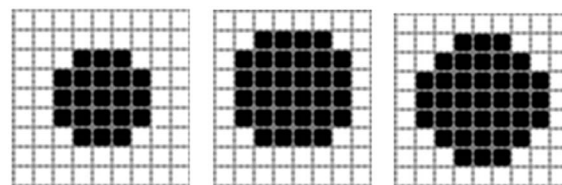


Fig. 3. Circular structural elements used for the smoothing operator: 5×5 , 6×6 , and 7×7 pixel size.

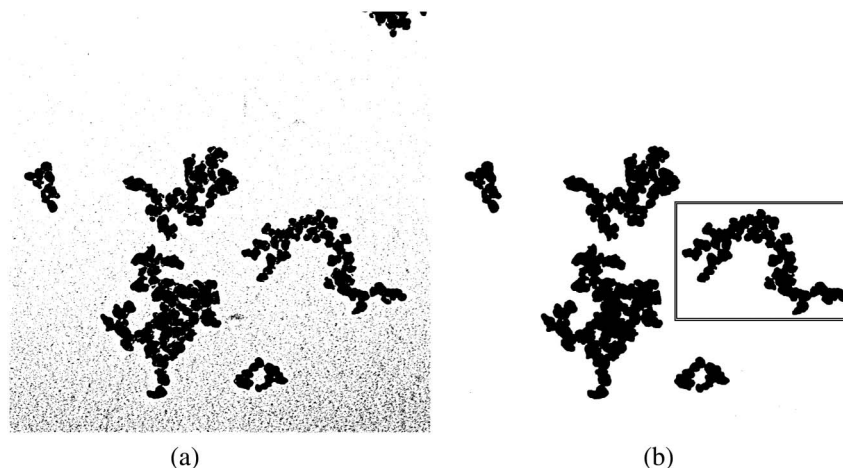


Fig. 4. (a) Output of Otsu thresholding. (b) Same after morphological smoothing and removal of border aggregates.

was chosen as the structural element for the rolling-ball transform.

In order to ensure that the smoothing element is independent of magnification, it is necessary to express it in a size other than pixels. The magnification of dataset A, for which these experiments were done, is 5600 \times , so the equivalent radius of the smoothing element is 4.85 nm. This sets the lower size limit of the objects that are detectable using the automated procedure for a magnification of 5600 \times . In a later section we will report measurements of the same sample that were made at a magnification of 17,000 \times . For that case, a smoothing element of 15 \times 15 pixels (4.71 nm radius) was chosen, which thus also satisfies the criteria given above.

For the identification of the primary particles comprising the aggregates, an edge-following algorithm based on Papert's turtle approach [35] was applied. This allows the identification of the edges of the aggregates as chains of pixels. For the sake of data reduction and convenience, the edges were vectorized in order to present the particle's border as a series of curve fragments stored as a 2D polygon. Figure 6(a)

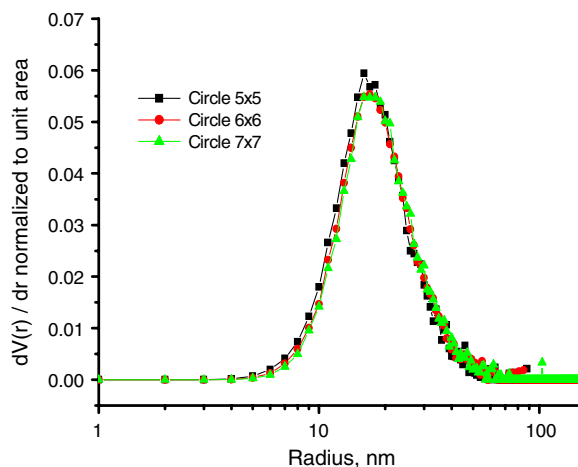


Fig. 5. (Color online) Size distribution of primary particles retrieved using different smoothing elements.

illustrates an example of the Papert turtle edge detection of the aggregate identified in the white box in Fig. 1(b).

4. Identification of Primary Particles

The Hough transform [36,37] was used for this purpose. It is a widely used instrument for parametric recognition of known geometric shapes (curves like circles, lines, and ellipses) in digital images. For more information about the numerous variants of the

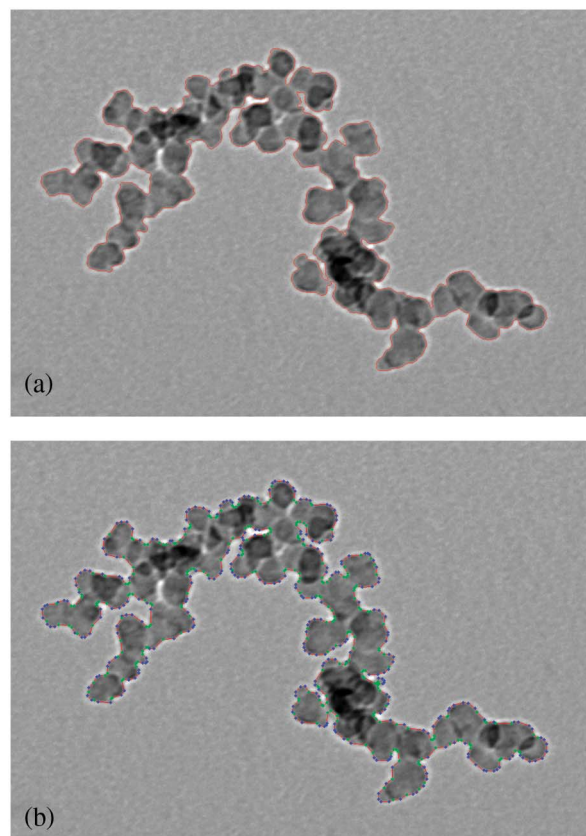


Fig. 6. (Color online) (Color online) (a) Outline of the aggregate, computed by Papert turtle algorithm and (b) same aggregate after edge vectorization.

Hough transform, see [34,38]. Most notable examples are the fast Hough transform [39], which addresses issues of storage and computational efficiency, the generalized Hough transform [40], which is designed to detect arbitrarily shapes on an image, and the probabilistic [41] and randomized [42] Hough approaches.

The original Hough transform relies on a parametric description of the equation of a curve and the evaluation of the parameters of the equation based on statistical analysis of the parameter space. The dimension of the parameter space is equal to the number of curve parameters. For example, in case of a straight line, there are two curve parameters; for a 2D circle, there are three; and so on. The statistical estimation of the parameters in the Hough method is improved by a so-called voting scheme [34]. Unfortunately, the Hough method has disadvantages. For example, its computational complexity is extremely high—worst case $O(N^2)$ [35], where the N is the size of the input image in pixels. This results from the need to compute all possible values of the curve parameters in the parameter space. Also, the memory required for the parameter matrix increases as N^p , where p is the number of parameters. For these reasons, the use of the Hough transform is practically impossible for processing high-resolution images [43].

To overcome this, the Hough transform algorithm [37] was modified. The modified algorithm looks for the points where the primary particles stick together and exploits them as a limiting condition in the parameter space search, thus reducing the problem of estimating the parameters of a sphere to one dimension (instead of three).

To reduce the time and memory cost of the calculations still further, the Hough transform was only applied to the output of the algorithm described in the previous section—i.e., to pixels of the image that belong to the exterior border of the aggregate.

The green circles in Fig. 7 show the result of applying the Hough transform to the border of the aggregate from Fig. 6. The thin red line shows the

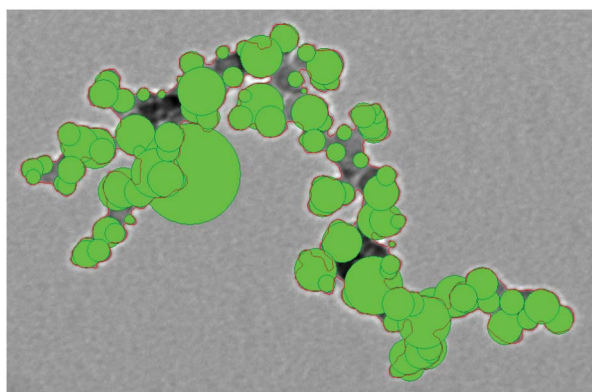


Fig. 7. (Color online) (Color online) Straightforward Hough transform of the particle's border.

particle's external border, as identified by the Papert turtle algorithm.

5. Regularization of the Solution

Unfortunately, the direct application of the Hough transform to the aggregate outline shown in Fig. 6(a) results in a significant number of artifacts. The main reasons for the appearance of these kinds of errors are as follows:

1. The presence of fragments on the aggregate's border that have a convex shape with very large radius of curvature: the Hough transform of such structures yields a single primary particle with a very large radius (e.g., left side of Fig. 7). To identify such errors quickly, the algorithm uses the Hough transform as an initial guess and checks whether more than 20% of the area of the initial guess lies outside the border of the aggregate. If so, it identifies the regions where the initial guess stays inside the border and uses these regions as a limit to adjust the initial guess so it fits within the projection of the aggregate. This occurred in more than 75% of the aggregates, mostly in the larger ones.

2. Large differences in the radius of curvature of the border of the aggregate: this is relatively rare, affecting less than 5% of the aggregates, but it complicates the estimation of the radius of the initial guess significantly, especially in the case of small nonspherical aggregates having very short border lengths. If the aggregate is too small to allow the reliable identification of its fragments, the algorithm simply replaces it with a sphere having an equivalent area of projection. If the aggregate is large enough, the algorithm locates the problem regions and replaces them by spheres of equivalent area, located in the center of the region.

In Fig. 8, the final output of the algorithm is overlaid on the original TEM image:

6. Implementation

The algorithm is very fast and does not require large computational resources. In the case reported here, it was implemented using the Borland C++ Builder

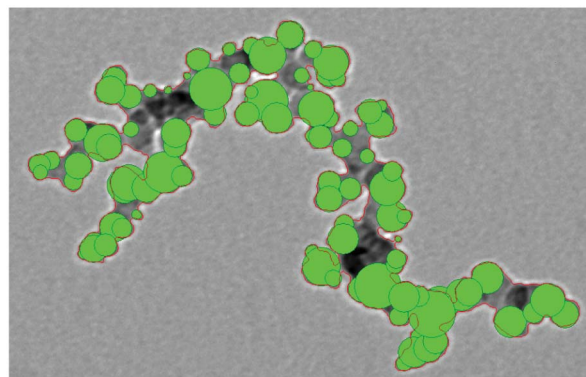


Fig. 8. (Color online) (Color online) Result shown in Fig. 7, after regularization of the Hough transform, overlaid on the original TEM image.

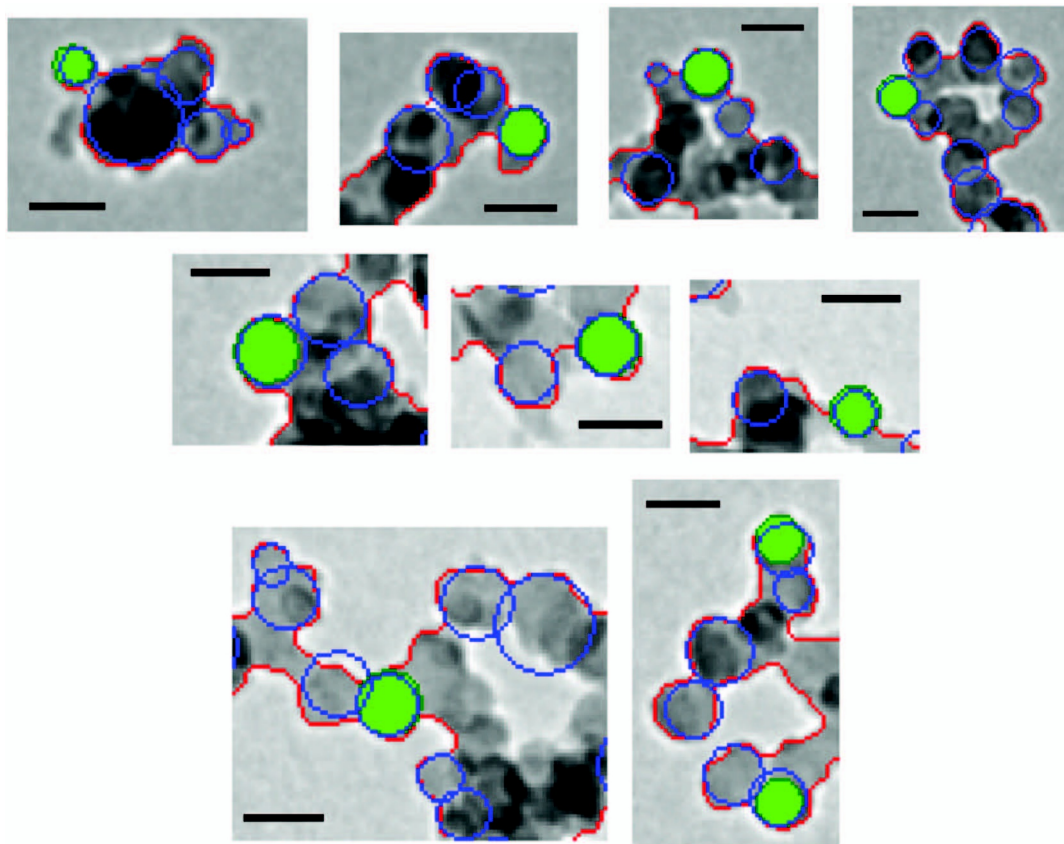


Fig. 9. Comparison of particles from the low-resolution dataset (A), measured by the automated method (blue circles) and by a human observer (green circles). The red curve outlines the border of the aggregate. The size of the black marker is 20 pixels (32 nm).

(version 5.0) development environment. The simulations were done using Microsoft Windows Vista Business on an Intel-based notebook with a Pentium dual-core CPU (2.53 GHz) and 2 GB of RAM. To optimize the calculation time, the C++ code was compiled and linked with the Fast Math library rather than the standard one and the executable was built with a graphic user interface based on Borland Visual Component Library components.

Using this configuration, the total processing time for 76 high-resolution images containing more than 3600 soot aggregates and involving the identification of more than 60,000 primary particles took about 70 min of CPU time. This can be improved further by compiling the code into separate dynamic link libraries without the functions that are not necessary for numerical processing (e.g., GUI and intermediate data output).

7. Validation of the Algorithm

In order to estimate the accuracy of the method, we have performed a comparison with the results of manual image processing.

In the first stage of the validation, we compared the measurements of primary particles by automated and manual procedures. Ten images were picked randomly from data array A, and on each image, some of the clearly visible primary particles were measured by a human observer. These were

processed by the automated image analysis independently.

Figure 9 presents some typical examples of the results of these measurements. Here, the perimeters of the particles identified and measured by the automated method are shown as blue circles, while those measured by the human observer are shown as filled green circles. The red curve outlines the border of the aggregate. This figure shows that for the cases where both methods were used to measure the same primary particle, the agreement is excellent.

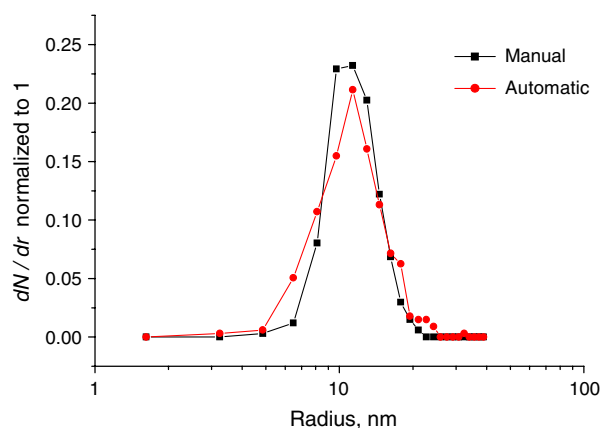
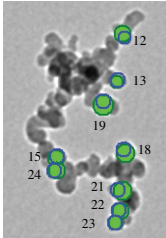


Fig. 10. (Color online) Comparison of manual and automated measurements of the primary particle radii.

Table 1. Comparison of Automatic and Manual Processing (Image 50mm-A3-5600X.0134)^a

	Index	Automatic Processing			Manual Processing		
		<i>x</i>	<i>y</i>	Radius	<i>x</i>	<i>y</i>	Radius
	(12)	175	88	14.6	177	92	11.3
	(13)	169	138	11.3	170	136	13.0
	(19)	155	162	17.8	155	158	13.0
	(18)	178	212	16.2	176	208	13.0
	(15)	106	217	14.6	107	215	13.0
	(24)	107	230	14.6	104	230	13.0
	(21)	175	251	16.2	170	250	13.0
	(23)	173	272	14.6	171	271	13.0
	(22)	168	284	13.0	167	284	13.0

^aBlue circles correspond to the primary particles identified by a human, and the circles filled with green correspond to the results of the automatic identification.

The quantitative results of this comparison are as follows. The 10 images from the low-magnification dataset (A) contained 479 aggregates. The automated process identified 10,300 primary particles in these aggregates, finding a mean radius of 14.7 ± 0.05 nm (standard deviation 5.4 nm). From the same 10 images, human observers measured 375 primary particles, finding a mean radius of 12.5 ± 0.2 nm (standard deviation 2.5 nm). Of the 375 primary particles measured by the human observer, the automated procedure identified and measured 366 finding a mean radius of 13.2 ± 0.2 nm. The size distributions obtained by the human and automated measurements of the 375- and 366-member subsets are given in Fig. 10.

From the comparison of the validation subsets we conclude that the detection rate of our approach is higher than 95%. Most of this difference was caused by primary particles that were located in the internal regions of the soot aggregates. These were missed by the algorithm because they had no contact with the external border, but were included in the human measurement. The missed particles are relatively rare and do not significantly change the shape of the retrieved size distribution or the average radius of the retrieved primary particles.

The average error of the location estimation is no more than 1–2 pixels (for the low-resolution dataset, the value corresponds to 1.6–3.24 nm), which is around 0.05%–0.1% of the dimension of the soot aggregate or 10%–20% of the average radius of the primary particle (see Fig. 9).

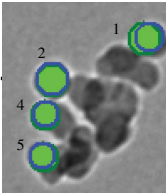
In the second stage of the validation, three images with clearly visible external outlines were selected

from data array A. The primary particles in each image were identified manually, and the radius and position of each were compared with the output of the algorithm. The results of the comparison are presented in Tables 1–3. All dimensions are given in nanometers; the magnification is 1.62 nm/pixel (5600 \times). The index that identifies each primary particle is given in the first column of each table. It can be seen that the differences between the manual and automated measurements of both radius and location are no more than 2 pixels (3.24 nm), indicating that the automated procedure works extremely well for these complicated agglomerates.

8. Comparison of Volume Distributions for Different Magnifications

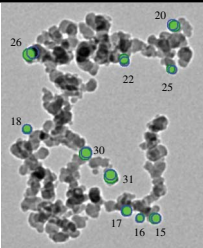
The volume distributions retrieved by the automated procedure are plotted in Fig. 11 for low-magnification dataset A (black) and high-magnification dataset B (red). The radius of the smoothing operator is 6×6 pixels or 4.85 nm for dataset A (magnification 5600) and 15×15 pixels or 4.71 nm for dataset B (magnification 17,000). These smoothing operators yield radii for the minimum measurable objects of 4.8 and 4.7 nm for the two datasets, so the plot has been truncated at a radius of 4 nm. Although the statistics are not as good for dataset B as for dataset A due to the smaller number of particles, it is clear that both distributions have the same shape. (This is expected because the samples came from images of the same TEM grids.) The automated procedure found an average primary particle radius of 14.5 ± 0.02 nm in the low-magnification sample and an average radius of 14.3 ± 0.1 nm for the primary

Table 2. Comparison of Automatic and Manual Processing (Image 50mm-A3-5600X.0133)^a

	Index	Automatic Processing			Manual Processing		
		<i>x</i>	<i>y</i>	Radius	<i>x</i>	<i>y</i>	Radius
	(1)	92	48	16.2	95	47	14.6
	(2)	37	73	16.2	37	72	16.2
	(4)	33	94	14.6	33	93	13.0
	(5)	32	119	14.6	31	118	13.0

^aBlue circles correspond to the primary particles identified by a human, and the circles filled with green correspond to the results of the automatic identification.

Table 3. Comparison of Automatic and Manual Processing (Image 50mm-A3-5600X.0134)^a

	Index	Automatic Processing			Manual Processing		
		<i>x</i>	<i>y</i>	Radius	<i>x</i>	<i>y</i>	Radius
	(20)	293	64	14.6	290	62	14.6
	(26)	63	109	16.2	69	106	16.2
	(22)	213	116	13.0	214	120	13.0
	(25)	287	132	11.3	290	133	11.3
	(18)	60	226	11.3	60	227	13.0
	(30)	147	266	16.2	154	264	14.6
	(31)	192	302	17.8	192	299	14.6
	(17)	218	356	13.0	217	356	14.6
	(16)	239	367	11.3	238	368	11.3

^aBlue circles correspond to the primary particles identified by a human, and the circles filled with green correspond to the results of the automatic identification.

particles in the high-magnification sample. In contrast to this, a human observer found a mean primary particle radius of 12.5 ± 0.2 for the primary particles in the low-magnification dataset and a value of 14.7 ± 0.1 nm for the particles in the high-magnification images.

A possible problem in the proposed technique may be related to the morphological smoothing (Fig. 3), which, during the preprocessing stage, eliminates tiny image features that would contribute to the fraction of primary particles having radius less than the size of the smoothing kernel (4.8 nm). Unfortunately, it is very difficult to estimate (even manually) the contribution of such particles to the measured size distribution because of their small size in comparison to much larger particles that might be nearby. The possible solution of the problem may be found by the incorporation of superresolution image processing methods [44]. This is being considered for future versions of the algorithm.

It is not clear why the human observer found a significantly smaller primary particle size at lower magnification. This is even more puzzling in view of the good agreement between human and automated measurements for all other datasets and for the tests reported in previous sections of this paper. Speculation on the reason for this is beyond the scope

of this work, because it could involve psychological as well as experimental biases, but we hope to examine this in future studies, if suitable experiments can be devised to test it.

9. Comparison with a Traditional Technique

While the relationship in Eq. (1) is considered to be one of the fundamental relations, in some experimental studies, it has been suggested [27,28] that the number of primary particles N in the aggregate is proportional to its projected area ($5 < N < 250$):

$$N = \left(\frac{A_{\text{aggregate}}}{A_{\text{monomer}}} \right)^\alpha, \quad (2)$$

where N is the number of the primary particles, $A_{\text{aggregate}}$ is the projected area of the aggregate, A_{monomer} is the projected area of the primary particle, and α is an empirical constant depending on the overlap parameter of the primary particles.

This simple relationship has been extensively studied [26,27] as a function of the fractal prefactor and overlap parameter C_{ov} of the primary particles in the aggregate. Thus, Eq. (2) estimates the total number of primary particles in the 3D structure of the soot aggregate and the constant α accounts for the 2D screening effect [45].

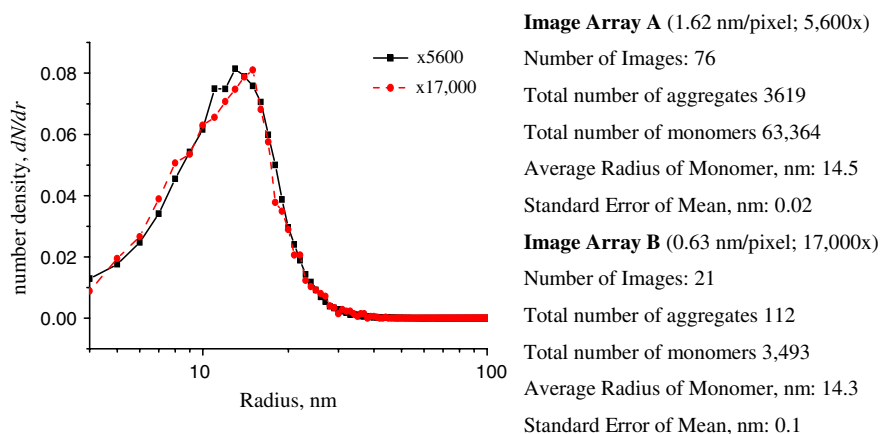


Fig. 11. (Color online) Automated measurements of the size distributions of primary particles in images with resolution 1.62 nm/pixel (5600 \times —image array A) and 0.63 nm/pixel (17,000 \times —image array B).

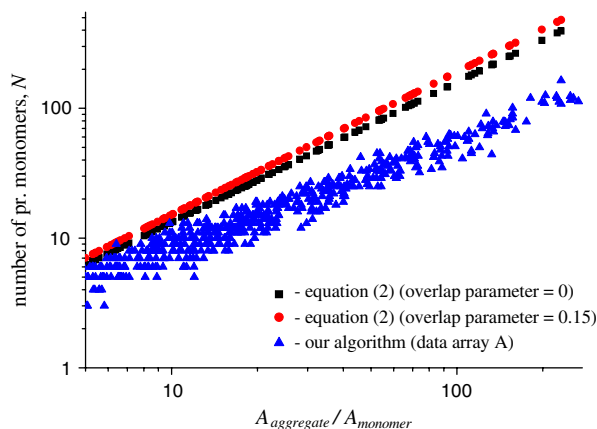


Fig. 12. (Color online) Number of primary particles as a projected area ratio.

In order to use the relationship, we estimated a value of 0.029 ± 0.001 for the overlap parameter C_{ov} of the primary particles in image array A. For the calculation of C_{ov} and $A_{aggregate}$, we exploited a computational technique described in [26]. The projected area of primary the particle $A_{monomer}$ was calculated as

$$A_{monomer} = \pi a^2,$$

where a is the average radius of the primary particles, retrieved in the total statistical ensemble.

Figure 12 shows the number of particles N retrieved by our algorithm in comparison with results predicted by Eq. (2), using parameters estimated by means of a procedure given in [26].

The total number of primary particles retrieved by our method (blue triangles) is significantly smaller than the estimates given by the equation because our experimental technique (2D imaging) cannot provide information along the third dimension and our numerical approach uses only the visible parts of the primary particles on the external border of the aggregate's projection. While our method does not retrieve and size *all* primary particles from the 2D image of the aggregate, the linearity of our results suggests

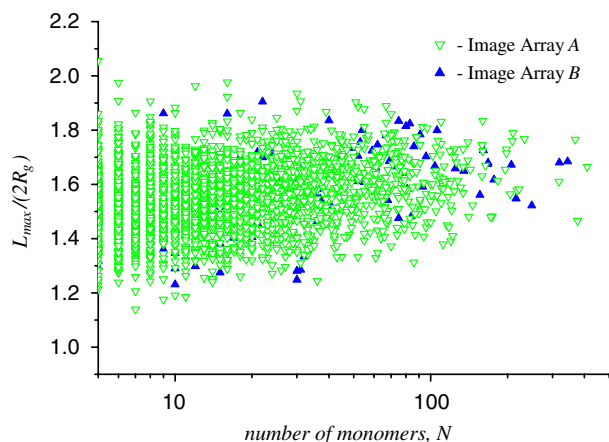


Fig. 13. (Color online) Ratio of maximum dimension to the radius of gyration of the aggregate for data array A.

that Eq. (2) gives a reasonable upper limit for the value of N .

Another step in the validation of our algorithm included calculation of the dimensionless parameter:

$$L_{max}/2R_g,$$

where R_g is the radius of gyration of the aggregate and L_{max} is the size of the aggregate along its maximum dimension.

Previous studies report the mean value of this parameter for different values of N as 1.5 ± 0.05 [26], and 1.49 (no confidence intervals reported) [27]. Figure 13 shows the values of $L_{max}/2R_g$ calculated for both image arrays. The average is 1.545 ± 0.002 (image array A) and 1.545 ± 0.01 (image array B), which is in excellent agreement with the conventional methods. The difference in the standard errors comes mainly from the difference in the statistical volume.

10. Conclusion

Soot nanoparticles are ubiquities in the urban environment, where they are very hazardous for human health. They are also transported over large distances in the troposphere, affecting radiative transfer, cloud nucleation, and precipitation. Quantification of these particles is therefore extremely important to many areas of science. Their complex shapes and variable composition, however, make their characterization difficult by any means other than direct human observation, which is prohibitively expensive because of their small size, highly variable shapes, and the large numbers of particles needed to get good statistics.

We report here a method for the automatic measurement of the sizes and shapes of soot aggregates. Unlike previously reported techniques, the algorithm begins with the location and sizing of the primary elements of the aggregate, and then it builds a mathematical model of the particle by means of a modified Hough transform of the fragments on the aggregate's boundary. The principal advantage of this approach is its ability to retrieve the details of the particles' morphology with very high accuracy. It also has general applicability to any irregularly shaped particles, so it has wide applicability for the processing of TEM and other kinds of particle images.

The algorithm presented here uses only the border of the aggregate and assumes spherical shapes for the primary particle elements. This simple approach is rapid, and the report presented here shows that it yields very accurate results. It is thus applicable to the rapid characterization of soot particles from environmental measurements. In future developments, we will improve the performance by inclusion of information from the internal regions of the aggregate. Assumed particle shapes will also be generalized for cases where this is appropriate, such as for mineral dust or pollen particles, for which the elemental shapes are either known or measurable.

References

1. S. K. Satheesh and K. K. Moorthy, "Radiative effects of natural aerosols: a review," *Atmos. Environ.* **39**, 2089–2110 (2005).
2. M. Strak, H. Boogaard, K. Meliefste, M. Oldenwening, M. Zuurbier, B. Brunekreef, and G. Hoek, "Respiratory health effects of ultrafine and fine particle exposure in cyclists," *Occup. Environ. Med.* **67**, 118–124 (2010).
3. A. K. K. Virtanen, J. M. Ristimäki, K. M. Vaaraslahti, and J. Keskinen, "Effect of engine load on diesel soot particles," *Environ. Sci. Technol.* **38**, 2551–2556 (2004).
4. S. C. Choi, H. G. Roh, K. S. Lee, and C. S. Lee, "Effects of fuel injection parameters on the morphological characteristics of soot particulates and exhaust emissions from a light-duty diesel engine," *Energy Fuels* **24**, 2875–2882 (2010).
5. M. Lapuerta, R. Ballesteros, and F. J. Martos, "The effect of diesel engine conditions on the size and morphology of soot particles," *Int. J. Veh. Des.* **50**, 91–106 (2009).
6. M. D. Hays, L. Beck, P. Barfield, R. J. Lavrich, Y. J. Dong, and R. L. Vander Wal, "Physical and chemical characterization of residential oil boiler emissions," *Environ. Sci. Technol.* **42**, 2496–2502 (2008).
7. P. M. Dakhel, S. P. Lukachko, R. C. Miake-Lye, R. C. Brown, and I. A. Waitz, "Post-combustion evolution of soot properties in an aircraft engine," in *Proceedings of GT2005: ASME Turbo Expo 2005* (ASME, 2005), Vol. 2, pp. 787–795.
8. N. Oshima, M. Koike, Y. Zhang, and Y. Kondo, "Aging of black carbon in outflow from anthropogenic sources using a mixing state resolved model: 2. Aerosol optical properties and cloud condensation nuclei activities," *J. Geophys. Res. Atmos.* **114**, D18202 (2009).
9. Z. B. Shi, D. Z. Zhang, H. Z. Ji, S. Hasegawa, and M. Hayashi, "Modification of soot by volatile species in an urban atmosphere," *Sci. Total Environ.* **389**, 195–201 (2008).
10. R. Y. Zhang, A. F. Khalizov, J. Pagels, D. Zhang, H. X. Xue, and P. H. McMurry, "Variability in morphology, hygroscopicity, and optical properties of soot aerosols during atmospheric processing," *Proc. Natl. Acad. Sci. USA* **105**, 10291–10296 (2008).
11. A. Kiselev, C. Wennrich, F. Stratmann, H. Wex, S. Henning, T. F. Mentel, A. Kiendler-Scharr, J. Schneider, S. Walter, and I. Lieberwirth, "Morphological characterization of soot aerosol particles during LACIS Experiment in November (LENo)," *J. Geophys. Res. Atmos.* **115**, D11204 (2010).
12. O. B. Popovicheva, E. D. Kireeva, M. A. Timofeev, N. K. Shonija, and V. P. Mogil'nikov, "Carbonaceous aerosols of aviation and shipping emissions," *Izv. Atmos. Ocean. Phys.* **46**, 339–346 (2010).
13. R. S. Stone, A. Herber, V. Vitale, M. Mazzola, A. Lupi, R. C. Schnell, E. G. Dutton, P. S. K. Liu, S. M. Li, K. Dethloff, A. Lampert, C. Ritter, M. Stock, R. Neuber, and M. Maturilli, "A three-dimensional characterization of Arctic aerosols from airborne Sun photometer observations: PAM-ARCMIP, April 2009," *J. Geophys. Res. Atmos.* **115**, D13203 (2010).
14. C. Adelhelm, R. Niessner, U. Poschl, and T. Letzel, "Analysis of large oxygenated and nitrated polycyclic aromatic hydrocarbons formed under simulated diesel engine exhaust conditions (by compound fingerprints with SPE/LC-API-MS)," *Analyt. Bioanal. Chem.* **391**, 2599–2608 (2008).
15. E. S. Cross, T. B. Onasch, A. Ahern, W. Wrobel, J. G. Slowik, J. Olfert, D. A. Lack, P. Massoli, C. D. Cappa, J. P. Schwarz, J. R. Spackman, D. W. Fahey, A. Sedlacek, A. Trimborn, J. T. Jayne, A. Freedman, L. R. Williams, N. L. Ng, C. Mazzoleni, M. Dubey, B. Brem, G. Kok, R. Subramanian, S. Freitag, A. Clarke, D. Thornhill, L. C. Marr, C. E. Kolb, D. R. Worsnop, and P. Davidovits, "Soot particle studies instrument inter-comparison project overview," *Aerosol Sci. Technol.* **44**, 592–611 (2010).
16. C. Asbach, H. Kaminski, H. Fissan, C. Monz, D. Dahmann, S. Mulhopt, H. R. Paur, H. J. Kiesling, F. Herrmann, M. Voetz, and T. A. J. Kuhlbusch, "Comparison of four mobility particle sizers with different time resolution for stationary exposure measurements," *J. Nanopart. Res.* **11**, 1593–1609 (2009).
17. A. F. Khalizov, H. X. Xue, L. Wang, J. Zheng, and R. Y. Zhang, "Enhanced light absorption and scattering by carbon soot aerosol internally mixed with sulfuric acid," *J. Phys. Chem. A* **113**, 1066–1074 (2009).
18. S. Suzuki, K. Kuwana, and R. Dobashi, "Effect of particle morphology on thermophoretic velocity of aggregated soot particles," *Int. J. Heat Mass Trans.* **52**, 4695–4700 (2009).
19. M. M. Maricq, "Bipolar diffusion charging of soot aggregates," *Aerosol Sci. Technol.* **42**, 247–254 (2008).
20. J. G. Slowik, E. S. Cross, J. H. Han, J. Kolucki, P. Davidovits, L. R. Williams, T. B. Onasch, J. T. Jayne, C. E. Kolb, and D. R. Worsnop, "Measurements of morphology changes of fractal soot particles using coating and denuding experiments: implications for optical absorption and atmospheric lifetime," *Aerosol Sci. Technol.* **41**, 734–750 (2007).
21. B. Hu, B. Yang, and U. O. Koylu, "Soot measurements at the axis of an ethylene/air nonpremixed turbulent jet flame," *Combust. Flame* **134**, 93–106 (2003).
22. K. A. Koehler, P. J. DeMott, S. M. Kreidenweis, O. B. Popovicheva, M. D. Petters, C. M. Carrico, E. D. Kireeva, T. D. Khokhlova, and N. K. Shonija, "Cloud condensation nuclei and ice nucleation activity of hydrophobic and hydrophilic soot particles," *Phys. Chem. Chem. Phys.* **11**, 7906–7920 (2009).
23. B. Karcher, O. Mohler, P. J. Demott, S. Pechtl, and F. Yu, "Insights into the role of soot aerosols in cirrus cloud formation," *Atmos. Chem. Phys.* **7**, 4203–4227 (2007).
24. C. H. Luo, W. M. Lee, and J. J. Liaw, "Morphological and semi-quantitative characteristics of diesel soot agglomerates emitted from commercial vehicles and a dynamometer," *J. Environ. Sci. China* **21**, 452–457 (2009).
25. A. F. Khalizov, R. Y. Zhang, D. Zhang, H. X. Xue, J. Pagels, and P. H. McMurry, "Formation of highly hygroscopic soot aerosols upon internal mixing with sulfuric acid vapor," *J. Geophys. Res. Atmos.* **114**, D05208 (2009).
26. A. M. Brasil, T. L. Farias, and M. G. Carvalho, "A recipe for image characterization of fractal-like aggregates," *J. Aerosol Sci.* **30**, 1379–1389 (1999).
27. U. O. Koylu, G. M. Faeth, T. L. Farias, and M. G. Carvalho, "Fractal and projected structure properties of soot aggregates," *Combust. Flame* **100**, 621–633 (1995).
28. R. J. Samson, G. W. Mulholland, and J. W. Gentry, "Structural analysis of soot agglomerates," *Langmuir* **3**, 272–281 (1987).
29. O. L. Gulder, D. R. Snelling, and R. A. Sawchuk, "Influence of hydrogen addition to fuel on temperature field and soot formation in diffusion flames," in *Twenty-Sixth Symposium (International) on Combustion* (Elsevier, 1996), Vol. 26, pp. 2351–2358.
30. P. S. Liao, Chen, T.-S. Chung, and P.-C. Chung, "A fast algorithm for multilevel thresholding," *J. Inf. Sci. Eng.* **17**, 713–727 (2001).
31. N. Otsu, "A threshold selection method from gray-level histogram," *IEEE Trans. Syst. Man Cybern.* **SMC-9**, 62–66 (1979).
32. J. N. Kapur, P. K. Sahoo, and A. K. C. Wong, "A new method for gray-level picture thresholding using the entropy of the histogram," *Comput. Vis. Graph. Image Proc.* **29**, 273–285 (1985).
33. J. P. Serra, *Image Analysis and Mathematical Morphology* (Academic, 1982).
34. E. R. Davies, *Machine Vision* (Elsevier, 2005).
35. I. Pitas, *Digital Image Processing Algorithms* (Prentice-Hall, 1993).
36. P. V. C. Hough, "Method and means for recognizing complex patterns," U.S. patent 3,069,654 (18 December 1962).
37. R. O. Duda and P. E. Hart, "Use of the Hough transform to detect lines and curves on pictures," *Commun. ACM* **15**, 11–15 (1972).
38. V. F. Leavers, "Which Hough transform?" *CVGIP Image Understand.* **58**, 250–264 (1993).
39. H. W. Li, M. A. Lavin, and R. J. Lemaster, "Fast Hough transform—a hierarchical approach," *Comput. Vision Graph. Image Proc.* **36**, 139–161 (1986).
40. D. H. Ballard, "Generalizing the Hough transform to detect arbitrary shapes," *Pattern Recogn.* **13**, 111–122 (1981).
41. R. S. Stephens, "Probabilistic approach to the Hough transform," *Image Vis. Comput.* **9**, 66–71 (1991).
42. L. Xu and E. Oja, "Randomized Hough transform (RHT): basic mechanisms, algorithms, and computational complexities," *CVGIP Image Understand.* **57**, 131–154 (1993).

- 43. S. Y. Guo, T. Pridmore, Y. G. Kong, and M. Zhang, "An improved Hough transform voting scheme utilizing surround suppression," *Pattern Recogn. Lett.* **30**, 1241–1252 (2009).
- 44. J. Tian and K. K. Ma, "A survey on super-resolution imaging," *Signal Image Video Process.* **5**, 329–342 (2011).
- 45. R. K. Chakrabarty, H. Moosmuller, W. P. Arnott, M. A. Garro, G. X. Tian, J. G. Slowik, E. S. Cross, J. H. Han, P. Davidovits, T. B. Onasch, and D. R. Worsnop, "Low fractal dimension cluster-dilute soot aggregates from a premixed flame," *Phys. Rev. Lett.* **102**, 235504 (2009).